Structural phase transitions in SrTiO₃ from deep potential molecular dynamics

Ri He [1,*] Hongyu Wu,[1,*] Linfeng Zhang,[2,3] Xiaoxu Wang,[2,3] Fangjia Fu,[3,4] Shi Liu [5,6,7,†] and Zhicheng Zhong [1,8,‡]

[1]*Key Laboratory of Magnetic Materials Devices & Zhejiang Province Key Laboratory of Magnetic Materials and Application Technology,*
Ningbo Institute of Materials Technology and Engineering, Chinese Academy of Sciences, Ningbo 315201, China
[2]*DP Technology, Beijing 100080, China*
[3]*AI for Science Institute, Beijing 100080, China*
[4]*School of Mathematical Sciences, Peking University, Beijing 100871, China*
[5]*School of Science, Westlake University, Hangzhou, Zhejiang 310024, China*
[6]*Institute of Natural Sciences, Westlake Institute for Advanced Study, Hangzhou, Zhejiang 310024, China*
[7]*Key Laboratory for Quantum Materials of Zhejiang Province, Hangzhou, Zhejiang 310024, China*
[8]*China Center of Materials Science and Optoelectronics Engineering, University of Chinese Academy of Sciences, Beijing 100049, China*

Strontium titanate (SrTiO₃) is regarded as an essential material for oxide electronics. One of its many remarkable features is the subtle structural phase transition, driven by the antiferrodistortive lattice mode, from a high-temperature cubic phase to a low-temperature tetragonal phase. Classical molecular dynamics (MD) simulation is an efficient technique to reveal atomistic features of phase transition, but its application is often limited by the accuracy of empirical interatomic potentials. Here, we develop an accurate deep potential (DP) model of SrTiO₃ based on a machine learning method using data from first-principles density functional theory (DFT) calculations. The DP model has DFT-level accuracy, capable of performing efficient MD simulations and accurate property predictions. Using the DP model, we investigate the temperature-driven cubic-to-tetragonal phase transition and construct the in-plane biaxial strain-temperature phase diagram of SrTiO₃. The simulations demonstrate that the strain-induced ferroelectric (FE) phase is characterized by two order parameters, FE distortion and antiferrodistortion, and the FE phase transition has both displacive and order-disorder characters. In this paper, we lay the foundation for the development of accurate DP models of other complex perovskite materials.

I. INTRODUCTION

Perovskite oxides with the formula ABO_3 is an important class of functional materials. In the ABO_3 perovskite structure, the A site cation is 12-fold coordinated, and the B site cation is sixfold coordinated with oxygen anions, respectively. Many different cations and anions can be incorporated in this structure, resulting in many functional materials that hold great promise for electronic device applications [1–3]. Strontium titanate (SrTiO₃, STO) as a representative ABO_3 perovskite oxide has long captured the attention of condensed matter physicists because of its rich physical properties such as two-dimensional electron gas [4–6], Rashba spin-orbit coupling [7–9], interfacial superconductivity [10,11], and multiple structural instabilities [12]. Among them, the incipient ferroelectricity is a unique structural property of STO that has attracted extensive studies [13–15]. At room temperatures, STO has a cubic structure with $Pm\bar{3}m$ space group. Below 105 K, it undergoes an antiferrodistortive (AFD) structural transition, transforming to a tetragonal $I4/mcm$ phase. The

AFD structure can be characterized by the neighboring TiO₆ octahedra rotating a small angle in the opposite directions around the [001] axis. The tetragonal phase is paraelectric (i.e., incipient ferroelectricity), where the quantum fluctuations and AFD instabilities suppress long-range polarization ordering. Despite the apparent paraelectric nature of STO, it exhibits many abnormal phenomena indicating its proximity to a ferroelectric (FE) phase [13,14]. Many experiments have demonstrated that the FE phase can be induced via various methods, including epitaxial strain from substrate [16,17], defect engineering [18], dimension reduction [19], cation doping [20], and optical and terahertz electric field excitation [21,22].

The tetragonal-to-cubic phase transition in STO has been intensively studied with the thermodynamic Landau-Ginsburg-Devonshire (LGD) model [23–26]. Nevertheless, the LGD model is often subjected to two well-known limitations: (i) the material coefficients involved in the Landau free energy expansion are difficult to determine, and a slight variance of the coefficient value may cause a drastic change of the resulting phase diagram [25]; (ii) such phenomenological models cannot reveal the mechanisms of phase transition at the atomic level. First-principles density functional theory (DFT) calculations can accurately predict the atomic structures of cubic and tetragonal phases of STO and their small energy difference (∼1.1 meV/atom) as well as the quantitative

---

*These authors contributed equally to this work.
†liushi@westlake.edu.cn
‡zhong@nimte.ac.cn

relationship between strain and polarization [27,28], but the expensive computational cost prevents the application of DFT from studying STO phase transition over a larger length and/or time scale (e.g., limited to a system of hundreds of atoms in the time scale of picoseconds). Classical molecular dynamics (MD) simulation is a very effective technique for understanding the structural phase transition mechanisms. Several empirical interatomic potentials have been developed to simulate the cubic structure of STO [29–31]. However, none of them have been used to explore the cubic-to-tetragonal phase transition, likely because the subtle energy variation (∼1 meV/atom) induced by the structural transition is beyond the energy resolution of the analytical function used to construct the interatomic potential [29]. Therefore, accurate MD simulations of phase transition in STO demands a high-accuracy potential.

In recent years, machine learning methods have been used as a powerful tool to develop the interatomic potential of crystalline and molecular materials. For instance, the Behler-Parrinello neural network [32], the Gaussian approximation potentials [33], the Select Neighbors and Parameters [34], and the SchNet [35] have achieved great success. Among them, the recently proposed deep potential (DP) model based on deep neural network can provide a DFT-level accurate interatomic potential by training from a large dataset of DFT energies and forces of a wide range of atomic configurations [36,37]. The well-trained deep-neural-network potential can be used to perform MD simulations without sacrificing the accuracy. In recent works, it has been demonstrated that the energy error of a DP model relative to DFT is within millielectronvolts per atom for the ground-state configuration [38–42]. Whether the DP model could describe the subtle free energy variation of just ∼1.1 meV/atom during tetragonal-to-cubic phase transition in STO remains a question.

In this paper, we develop an accurate DP model for STO based on a deep learning method trained on the data from DFT calculations. The accuracy of the DP models is examined by comparing with DFT results. The temperature-driven tetragonal-to-cubic phase transition of STO is well captured by DPMD simulations. Finally, the FE-paraelectric phase transition temperatures at different in-plane strains are calculated by the DP model, and the nature of FE phase transition is characterized at the atomic level. These DPMD simulation results provide atomistic insights into the microscopic ferroelectricity mechanism of STO under strain.

II. COMPUTATIONAL METHODS

A. Deep learning of interatomic potential of SrTiO$_3$

In the DP model, the potential energy E of a configuration is assumed to be a sum of each atomic energy E_i of atom i, which is mapped from a descriptor D_i through an embedding network. The descriptor D_i characterizes the local environment of atom i within a cutoff radius R_c. Here, the R_c is set to 6 Å. The maximum number of atoms within the R_c is set to 160 for Sr, 160 for Ti, and 480 for O, respectively. The translational, rotational, and permutation symmetry of the D_i are preserved by an embedding network. The smooth

edition of the DP model was employed to remove the discontinuity introduced by the cutoff radius [37]. The sizes of the embedding and fitting networks are (25, 50, 100) and (240, 240, 240), respectively. The residual network was employed in the training of fitting network. The loss function is defined as

$$L(p_\varepsilon, p_f, p_\xi) = p_\varepsilon \Delta \epsilon^2 + \frac{p_f}{3N} \sum_i |\Delta \mathbf{F}_i|^2 + \frac{p_\xi}{9} \|\Delta \xi\|^2, \quad (1)$$

where $\Delta \epsilon$, $\Delta \mathbf{F}_i$, and $\Delta \xi$ represent the energy, force, and virial tensor difference between the DP model prediction and the training dataset (from DFT calculations). The p_ε, p_f, and p_ξ are weight coefficients of energy, force, and virial tensor. The p_ε and p_ξ increase from 0.02 to 1, and p_f decreases from 1000 to 1 during the training procedure. The DP models are trained with 1 200 000 steps. These optimized hyperparameters have been proven to be able to reproduce the first-principles training database with sufficient accuracy for many materials such as Al-Mg alloy [42], HfO$_2$ [38], amorphous Li−Si alloy [43], two-dimensional In$_2$Se$_3$ [40], and condensed H$_2$O [44]. Therefore, we believe it is reasonable to use the same hyperparameters in the training process.

B. Generation of the training dataset

In this paper, we use the DP generator (DP-GEN) to generate a set of training data that covers a sufficient wide range of relevant configurational space efficiently [39]. DP-GEN is a concurrent learning procedure, and the workflow of each iteration includes three main steps: training, exploration, and labeling (see Fig. 1).

We start with DFT relaxed ground-state structures of $Pm\bar{3}m$ cubic and $I4/mcm$ tetragonal phase. The lattice constants calculated by DFT with Perdew-Burke-Ernzerhof solid (PBEsol) are shown in Table I. In the first iteration, the initial training dataset contains 200 randomly perturbed structures of $2 \times 2 \times 2$ $Pm\bar{3}m$ cubic and $1 \times 1 \times 1$ $I4/mcm$ tetragonal cell. The maximum magnitude of perturbed displacement is 0.01 Å for the atomic coordinates, and the maximum strain is 3% of the ground-state lattice parameters. Starting with these DFT training datasets, four DP models are trained, starting with different values of deep neural network parameters. Then the exploration step was performed in which one of the DP models is used for MD simulations to explore the configuration space at different temperatures. For all sampled configurations in MD trajectories, the other three DP models will predict the corresponding energies and atomic forces. The maximum deviation of the four DP model prediction of forces ($\sigma_f^{\max}$) can be used to formulate the criterion for labeling:

$$\sigma_f^{\max} = \max_i \sqrt{\langle |\mathbf{F}_i - \langle \mathbf{F}_i \rangle|^2 \rangle},$$

where $\langle \ldots \rangle$ indicates the average of model predictions. The configurations with $\sigma_f^{\max} < \sigma_{\text{low}}$ are already well represented by previous training datasets [green points in Fig. 1(e)], which are labeled as accurate configurations, whereas a configuration with a large model deviation $\sigma_f^{\max} > \sigma_{\text{high}}$ is highly distorted and unphysical due to poor model quality [red points in Fig. 1(e)] and is thus labeled as a failed configuration. Therefore, only configurations satisfying $\sigma_{\text{low}} < \sigma_f^{\max} < \sigma_{\text{high}}$ are labeled as candidates for further DFT calculations and are
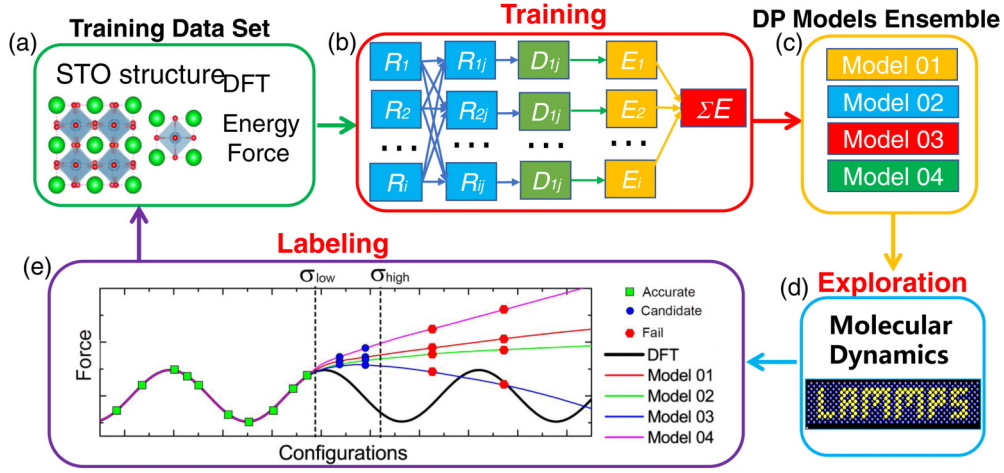
FIG. 1. Schematic illustration of the deep potential generator (DP-GEN) process, including training, exploration, and labeling. (a) The training dataset contains hundreds of perturbed structures and corresponding density functional theory (DFT) energies and forces. (b) Starting with these DFT training data set, (c) four DP models are trained starting with different values of deep neural network parameters. (d) Performing one of the DP models is used for molecular dynamics (MD) simulations to explore the configuration space at different temperatures. (e) Labeling selected candidates by DFT calculation and then added to the training dataset of next iteration.

added to the training dataset for training in the next iteration [blue points in Fig. 1(e)]. Here, σ_{low} and σ_{high} are set to 0.05 and 0.20 eV/Å, respectively, as suggested in the literature [39]. It is important to point out that σ_f^{max} can be also used as the convergence criterion for DP-GEN iterations. Here, the exploration of each system is considered converged when the percentage of accurate configurations ($\sigma_f^{\text{max}} < \sigma_{\text{low}}$) is >99%. For more details of the DP-GEN method, please refer to the literature [22].

C. DFT calculations setting

The initial training dataset is obtained by performing a 10-step *ab initio* MD simulation for randomly perturbed structures at 50 K. After labeling candidate configurations, self-consistent DFT should be performed. All DFT calculations were performed using a plane-wave basis set with a cutoff energy of 500 eV as implemented in the Vienna *Ab initio* Simulation Package (VASP) [45,46], and the electron exchange-correlation potential was described using the generalized gradient approximation and PBEsol scheme [47]. The Brillouin zone was sampled with a $6 \times 6 \times 6$ k-point grid for a $2 \times 2 \times 2$ $Pm\bar{3}m$ supercell and a $6 \times 6 \times 5$ k-point grid for

a $1 \times 1 \times 1$ $I4/mcm$ cell. Through the testing, the values of cutoff energy and k-point can capture a millielectronvolt-level energy difference between ground-state tetragonal and cubic phase (see Fig. S1 in the Supplemental Material [48]).

D. MD simulations setting

The MD simulations were carried out using LAMMPS code with periodic boundary conditions [49]. At the exploration step, MD simulations adopt the isobaric-isothermal (NPT) ensemble with temperature set from 50 to 400 K, pressure set from 0.001 to 50 kbar, and time with 2 to 20 ps (Table S1 in the Supplemental Material [48]). A Nose-Hoover thermostat and Parrinello-Rahman barostat are employed to control temperature and pressure, respectively [50,51]. After DP-GEN iteration is considered converged, the optimized DP models of STO can be used to study the structural transitions driven by temperature and strain via performing MD simulations. The NPT MD simulations starting with a ground-state tetragonal $I4/mcm$ $10 \times 10 \times 10$ pseudocubic supercell (5000 atoms) were performed with periodic boundary conditions and at zero pressure to model the temperature and strain-driven structural transition. The time step is set to 0.001 ps. Simulations using a $20 \times 20 \times 20$ supercell give similar results. At a specified temperature, the equilibrium run is 10 ps, followed by a production run of 90 ps (see Fig. S2 in the Supplemental Material [48]). The main results are not sensitive to the initial configuration ($Pm\bar{3}m$ or $I4/mcm$) for MD simulation. To apply a strain of ε_s, the in-plane lattice constant of the supercell was fixed at $a_0 + \varepsilon_s a_0$ Å, where a_0 is the optimized in-plane lattice constant of STO at the corresponding temperature, and the out-of-plane lattice constant was allowed to fully relax. After the thermodynamic equilibrium of supercells, the local pseudocubic cell polarization could be calculated by atomic displacements ($\mathbf{u}_i$) with respect to the referenced cubic phase multiplied by the Born effective charges ($\mathbf{Z}_i^*$):

$$P = \sum \mathbf{Z}_i^* \mathbf{u}_i.$$

TABLE I. The DFT (E^{DFT}) and DP energies (E^{DP}) of $Pm\bar{3}m$, $I4/mcm$, and $Pnma$ phases. $E^{Pm\bar{3}m} - E^{I4/mcm}$ and $E^{Pnma} - E^{I4/mcm}$ is the energy of $Pm\bar{3}m$ and $Pnma$ phases relative to the ground-state $I4/mcm$ phase.

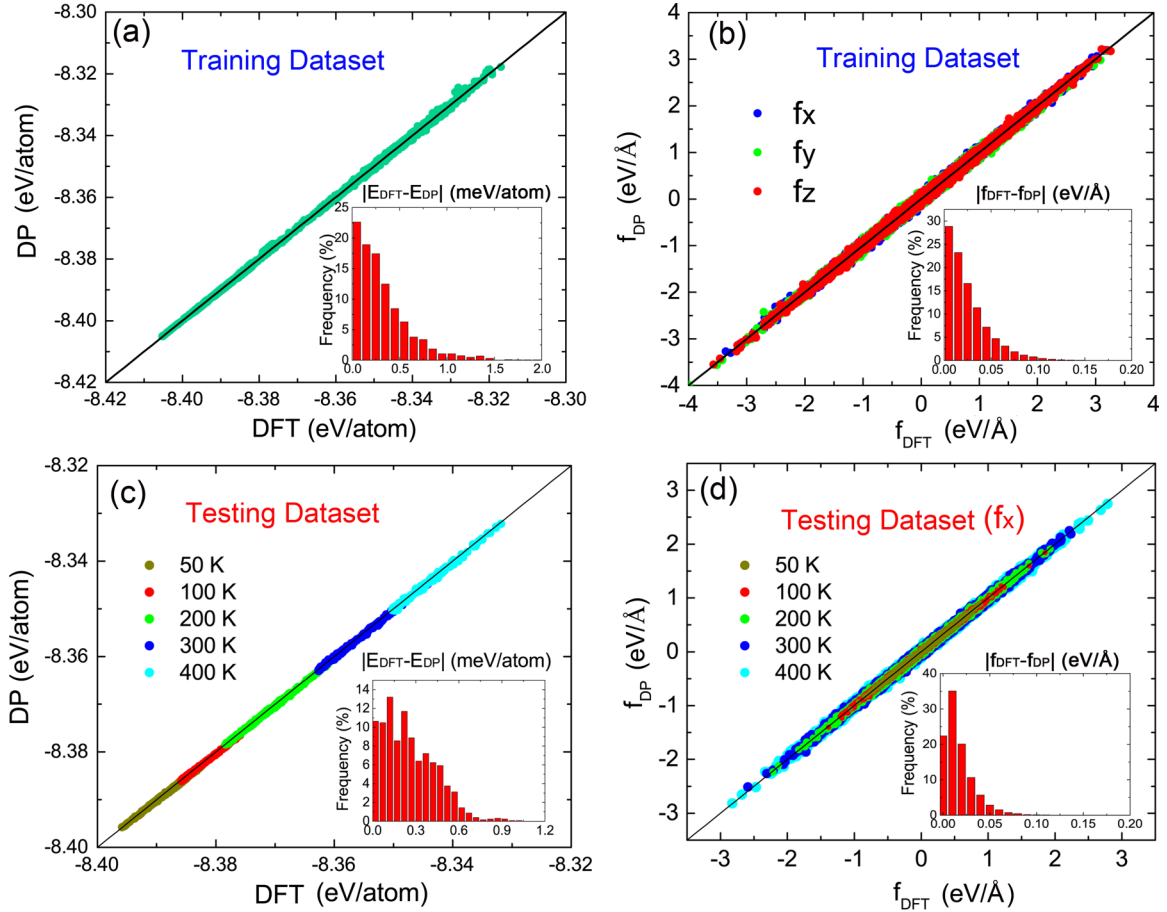| Structure	E^{DFT} (eV/atom)	E^{DP} (eV/atom)	Error (meV/atom)
$Pm\bar{3}m$	−8.404051	−8.403994	0.057
$I4/mcm$	−8.405148	−8.405002	0.146
$E^{Pm\bar{3}m} - E^{I4/mcm}$	0.001096	0.001008	0.09
$Pnma$	−8.360826	−8.361460	0.634
$E^{Pnma} - E^{I4/mcm}$	0.044322	0.043542	0.78

FIG. 2. Comparison of (a) and (c) energies and (b) and (d) atomic forces calculated using the deep potential (DP) model and density functional theory (DFT) calculation for all configurations in the (a) and (b) final training dataset and (c) and (d) testing dataset, respectively.

The components of Born effective charge tensors along the out-of-plane direction were obtained by DFT calculations: $Z_{Sr}^* = 2.54$, $Z_{Ti}^* = 7.12$, $Z_{O1}^* = -5.66$, $Z_{O2}^* = -2.00$, where O1 denotes the oxygen atom in the SrO layer, and O2 denotes the oxygen atom in the TiO$_2$ layer.

E. DP-GEN iteration process

The distributions of σ_f^{max} at different temperatures in the first five iterations are shown in Fig. S3 in the Supplemental Material [48], and the detailed percentage values of the accurate, candidate, and failed configurations in each iteration are shown in Table S1 in the Supplemental Material [48]. In the first iteration, starting with two systems of a $2 \times 2 \times 2$ $Pm\bar{3}m$ supercell (40 atoms) and a $1 \times 1 \times 1$ $I4mcm$ cell (20 atoms), a lot of the configurations were labeled as candidates (39.5%) and failed (16.8%) because the preliminary DP model is very rough due to the limited information in the training dataset. After adding hundreds of candidate configurations into the training dataset in the second iteration and a complete training, all sampled low-temperature configurations (50–200 K) were labeled as accurate, and candidate configurations come from higher-temperature simulations. To explore the wider configuration space, larger supercells are added at later exploration steps. The whole DP-GEN iteration process is started

with 400 initial configurations, then explored 3 million configurations. Finally, the 2600 candidate configurations were selected for labeling and added into the training dataset after a total number of 15 iterations. All settings of the exploration strategy are listed in Table S1 in the Supplemental Material [48].

III. RESULTS AND DISCUSSIONS

A. Accuracy of DP model

The model parameters are estimated using an optimization algorithm, which ensures the generality and transferability of DP models. We compare the energies and atomic forces calculated using the DP model and DFT calculations for the configurations in the final training dataset. As shown in Fig. 2, the mean absolute error of energy (ΔE^{DP-DFT}) and atomic force (ΔF^{DP-DFT}) between DP and DFT is 0.322 meV/atoms and 0.025 eV/Å, respectively. We also compare the DFT and DP results in a separate testing dataset of 1500 crystal configurations (80 atoms supercell) to validate the generalizability of the trained model. We find good agreement between DP predictions and DFT energies and forces with a mean absolute error of 0.26 meV/atom and 0.019 eV/Å for the testing dataset, demonstrating the generalizability of the trained DP model. The DFT and DP model energies of cubic $Pm\bar{3}m$ and tetragonal $Pm\bar{3}m$ phases are listed in Table I. For the

TABLE II. Lattice constants of $Pm\bar{3}m$ and $I4/mcm$ phase at 0 K predicted by DP model and DFT. φ is the rotation angle of the TiO$_6$ octahedra around [001].

Structure	Method	a, b/Å	c/Å	φ/°
$Pm\bar{3}m$	DFT	3.895	–	–
	DP	3.898	–	–
$I4/mcm$	DFT	3.885	3.906	5.49
	DP	3.888	3.910	5.49

structures of cubic and tetragonal phases relaxed by DP and DFT, the $\Delta E^{\text{DP-DFT}}$ is equal to 0.057 and 0.146 meV/atoms, respectively. The energy gain of a cubic phase relative to the ground-state tetragonal phase ($\Delta E^{\text{C-T}}$) is a key factor that determines the phase-transition temperature. The DFT calculated $\Delta E^{\text{T-C}}$ is 1.096 meV/atom, and the DP calculated value is 1.008 meV/atom. It demonstrates that the DP model can capture a millielectronvolt-level energy difference between ground-state tetragonal and cubic phases. It is also noted that the training dataset does not contain structural information of the orthorhombic $Pnma$ phase, but $\Delta E^{\text{DP-DFT}}$ for $Pnma$ STO is only 0.634 meV/atoms (Table I). It indicates that the DP model could calculate well the configurations which are not included in the training dataset.

Table II summarizes equilibrium lattice constants optimized by DP and DFT for two phases of STO at 0 K. The lattice constants for the DP model are within 0.004 Å of the DFT results. We also use the DP model to calculate the elastic constants for cubic and tetragonal phases and compare the values with DFT results. The results are shown in Table III, demonstrating great agreement between DP and DFT. The equations of state of the cubic phase calculated by DFT and DP model are presented in Fig. 3(a). The DP model reproduces well the DFT results over a wide range of lattice constants (3.7–4.0 Å). Adding more configurations of large lattice constants to the training dataset can further improve the DP model by fixing the slight deviation beyond 4.0 Å. Many experiments have demonstrated that the FE phase can be induced in STO via strain engineering [16,25,28]. We use

DP model to predict the energy variation of cubic phases under in-plane biaxial strain and polarization (i.e., off-centering displacement of Ti atom). The results are shown in Figs. 3(b) and 3(c), again demonstrating excellent agreement between DP and DFT results. We demonstrate that the DP model can accurately describe orthorhombic $Pnma$ phase STO, the information of which was not included in the training dataset. We further explore the structure-energy relationship along the phase transition trajectory from the $Pm\bar{3}m$ phase to the $Pnma$ phase by the DP model, and the DP results are in good agreement with DFT results, as shown in Fig. 3(d).

We also calculate the phonon dispersion relations and corresponding density of states of the cubic phase by the DP model and DFT. As shown in Fig. 4, the DP model calculated phonon dispersion of cubic STO agrees well with the DFT spectrum, showing multiple lattice instabilities, i.e., an unstable AFD zone-boundary R$_5^-$ mode that corresponds to concerted rotations of the oxygen octahedra, leading to the low-temperature tetragonal structure and an unstable zone-center polar Γ_4^- mode associated with the incipient ferroelectricity. The slight difference of the polar Γ_4^- mode at the Γ point between DP and DFT could be eliminated if adding configurations with atoms perturbed according to the polar Γ_4^- mode.

B. Temperature-driven phase transition

Using the DP model, the atomic structure of STO at the finite temperature can be determined from DPMD simulations. Considering the AFD of staggered octahedra rotation around [001] in the tetragonal phase, we define $\varphi_n = (-1)^n \theta_n$ as the AFD order parameter, where the index n is the sequence number of unit cell, and θ is the rotation angle of TiO$_6$ octahedra in each unit cell. The temperature-dependent lattice constants and φ are shown in Fig. 5. The simulated system has a tetragonal phase at low temperature. The sketch of AFD order parameter φ are shown in Fig. 6(a). As the temperature increases, both the tetragonal distortion (c/a) and φ decrease. The φ goes from a value of 4.61° at 50 K to 0.22° at 200 K. To get the atomistic insights into the phase transition, the distributions of φ within each unit cell at different temperatures are shown in Fig. 6. It is indicated that the tetragonal phase has a long-range AFD ordering pattern at low temperature and that the long-range feature vanishes at higher temperature, where we observed short-range AFD ordering patterns appearing dynamically in space at 200 K [see Fig. 6(d)]. According to the variation of the lattice constant and φ, the transition from tetragonal to cubic phase takes place when the temperature is raised >190 K. The DP model predicted behavior of temperature-driven phase transition in STO is in qualitative agreement with experiment, but the transition temperature is slightly higher than the experimental value of 105 K [52]. In addition, DPMD predicts a linear behavior of a- and b-axis lattice constants at low temperature, whereas the saturated temperature dependence of the lattice parameter <50 K was observed in the experiment [53]. At present, we can think of two possible explanations for the disagreements between experiment and simulation: (i) the systematic error of the energy difference between two phases from DFT calculation, for example, the energy difference between two phases is

TABLE III. The elastic constants, bulk modulus (Bv), shear modulus (Gv), and Poisson's ratio (v) predicted by DP model and DFT. The unit of modulus is GPa.

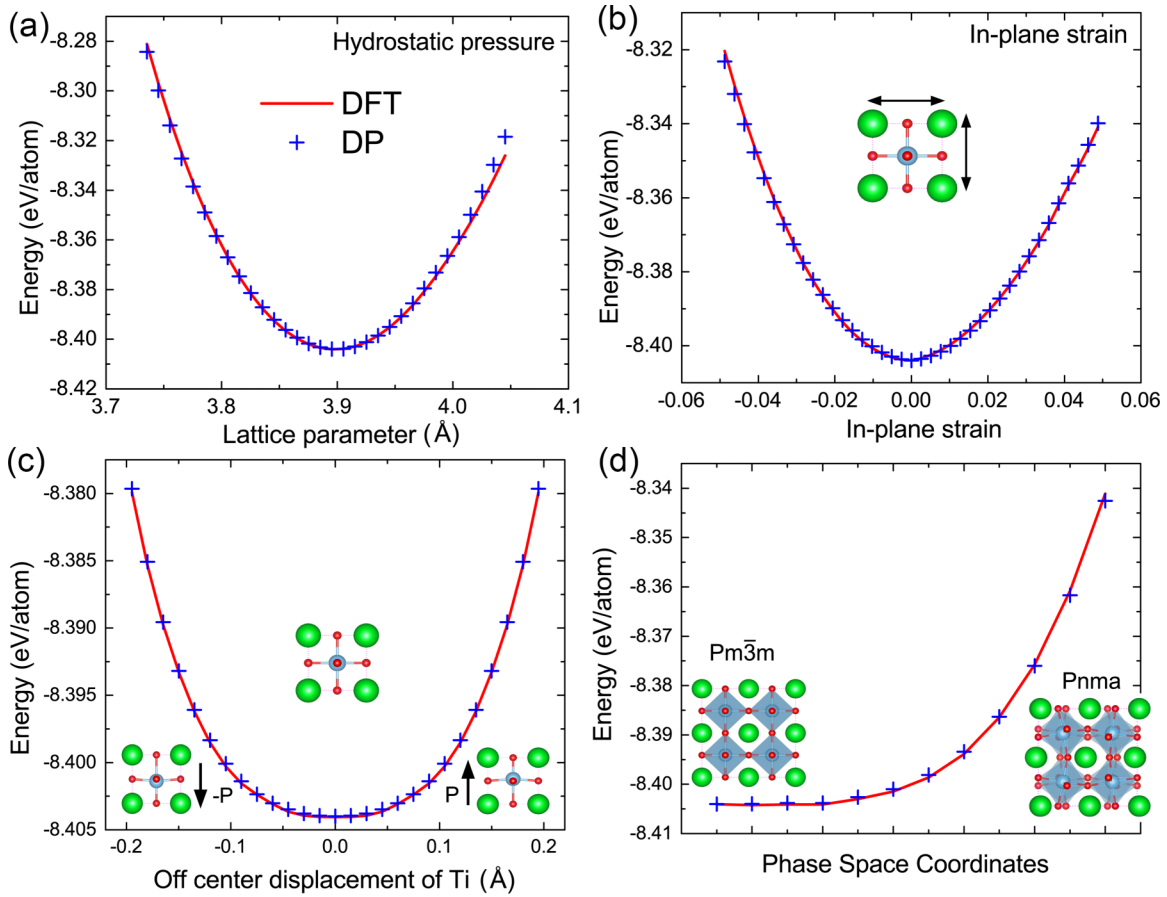|	Cubic $Pm\bar{3}m$		Tetragonal $I4/mcm$	
	DFT	DP	DFT	DP
Bv	173	182.29	173	187.68
Gv	110	100.89	109	102.91
V	0.24	0.23	0.25	0.247
C_{11}	351.93	363.18	352.23	337.752
C_{12}	104.74	106.85	103.38	88.561
C_{44}	116.28	100.89	115.99	99.766
C_{33}	–	–	357.15	344
C_{13}	–	–	107.87	123.01
C_{66}	–	–	115.95	109.2

FIG. 3. The deep potential (DP) model and density functional theory (DFT) calculated energies for (a) hydrostatic pressure, (b) in plane strain, (c) Ti atom displacement of cubic phase, and (d) phase transition trajectory from cubic $Pm\bar{3}m$ to orthorhombic $Pnma$ phase. It should be noted that the $Pnma$ phases are not included in the training dataset of the DP model.

pseudopotential dependent; (ii) more likely, MD simulation does not include any quantum nuclear effects. Standard MD simulation treats the atomic nuclei as pointlike classical particles and explores the phase space of a system by classical equations of motion. We know, however, that the nuclei are quantum objects, and they satisfy the Bose-Einstein statistics. The equation of nuclei motion should be rewritten as

Langevin type rather than classical type in MD simulation [54–56]. Previous work has shown that the quantum nuclear effects can reduce the phase-transition temperature of STO by
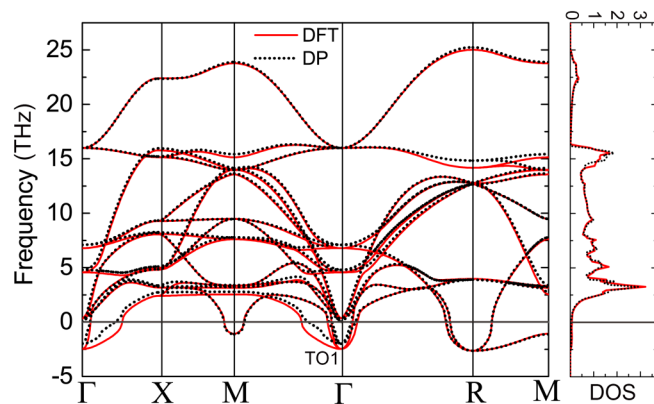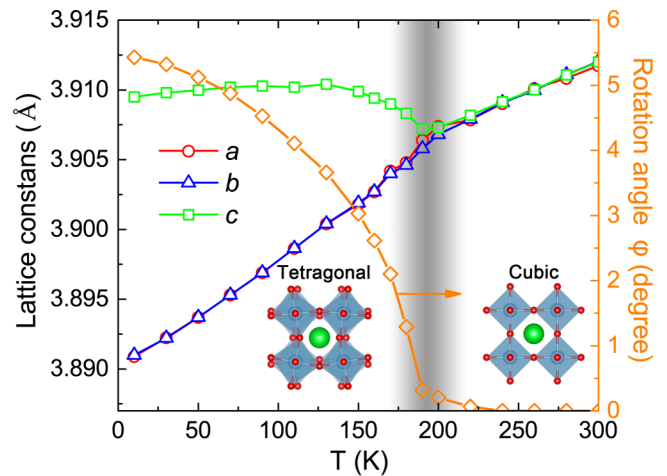

FIG. 4. The phonon dispersion relations and density of states of cubic $Pm\bar{3}m$ phase of STO calculated by deep potential (DP) model and density functional theory (DFT).

FIG. 5. Average lattice constants and rotation angle of the TiO$_6$ octahedra around [001] (φ) for SrTiO$_3$ as a function of temperature determined from deep potential molecular dynamics (DPMD) simulations with a 5000-atom supercell.

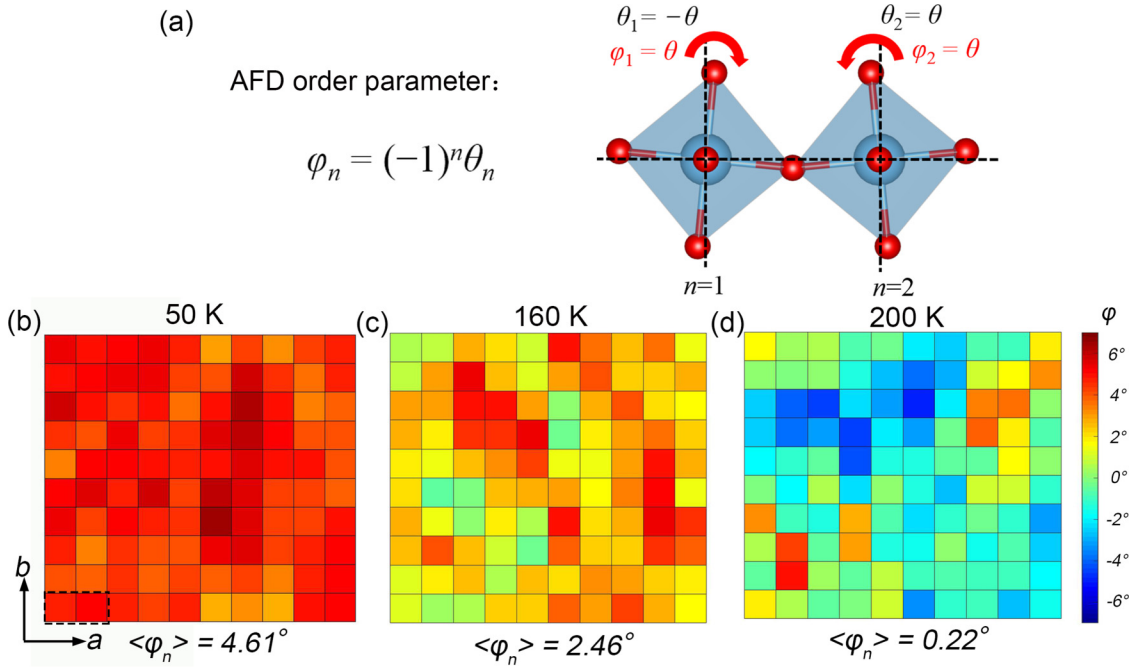FIG. 6. Sketch of (a) the antiferrodistortive (AFD) order parameter φ and the distribution of φ within each unit cell in the *ab* plane (in plane) at temperature of (b) 30 K, (c) 160 K, and (d) 200 K (d). The color illustrating the magnitude of φ.

35 to 50 K [15]. Therefore, adding the nuclear quantum effects into MD simulation (e.g., Path Integral MD or Quantum Thermal Bath MD) may eliminate the disagreement between experiment and simulation.

C. Strain effect

It is well known that STO is an incipient FE so that the FE transition does not appear under the strain-free state even when temperature decreases to 0 K. It is generally believed the FE order is suppressed by quantum fluctuation [14,15] and preceding AFD distortion [12,57]. No matter what type of reason it was, the situation may change dramatically in the strained state. Many theoretical works and experiments reported epitaxial strain could induce a polar or FE phase in STO films [16,17,24–26,28]. Here, we predict the in-plane biaxial strain-temperature phase diagram of STO using DPMD simulations.

Figure 7 shows the phase diagram of FE and AFD phases as a function of temperature and in-plane biaxial strain for STO by DPMD. Here, we use two order parameters, the average polarization (P) and the AFD order parameter (φ), to distinguish the pure FE, FE, AFD, and paraelectric phases: the pure FE phase is defined as $P \neq 0$ and $\varphi = 0$, the FE phase is defined as $P \neq 0$ and $\phi \neq 0$, the AFD phase is defined as $P = 0$ and $\varphi \neq 0$, whereas the paraelectric phase is defined as $P = 0$ and $\varphi = 0$. After the thermodynamics equilibrium of the supercell, the local P of the pseudocubic cell could be roughly defined by atomic displacements with respect to the referenced cubic phase (for details, see Computational Methods). It is seen that the FE phase becomes the most stable phase when the compressive (only when >0.2%) and tensile strain was applied. At low temperatures, the compressive strain can induce the out-of-plane P and AFD structure with

rotation axis along [001], whereas the tensile strain induces the in-plane P and AFD structure with rotation axis along [100] and [010] (for structural details, see Figs. S4 and S5 in the Supplemental Material [48]). Then the FE phase transfers to the AFD structural phase when the temperature increases. It is clear to see that the FE transition temperature increases with the in-plane strain. When further increasing temperature, the AFD structure phase will transform to the paraelectric phase with P and φ both decreased to zero. The phase diagram from the DP model reveals the temperature of the FE
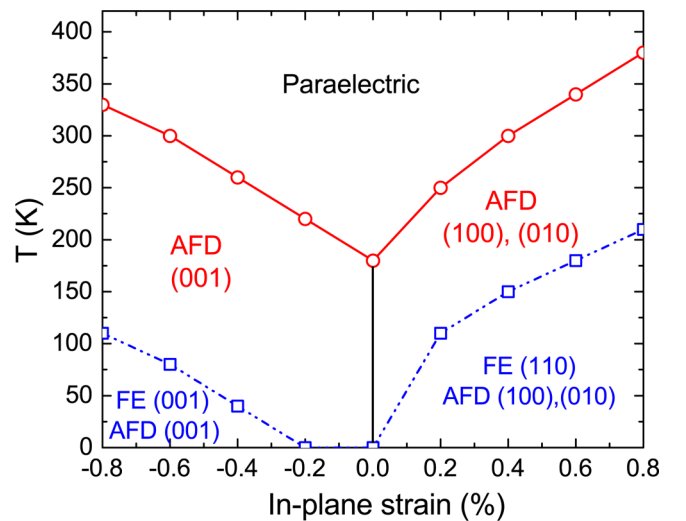

FIG. 7. Predicted phase diagram of bulk SrTiO$_3$ under biaxial in-plane strain by deep potential molecular dynamics (DPMD) simulations. Ferroelectric and antiferrodistortive (AFD) transition temperature are plotted by blue square dot and red dot at different strains, respectively.
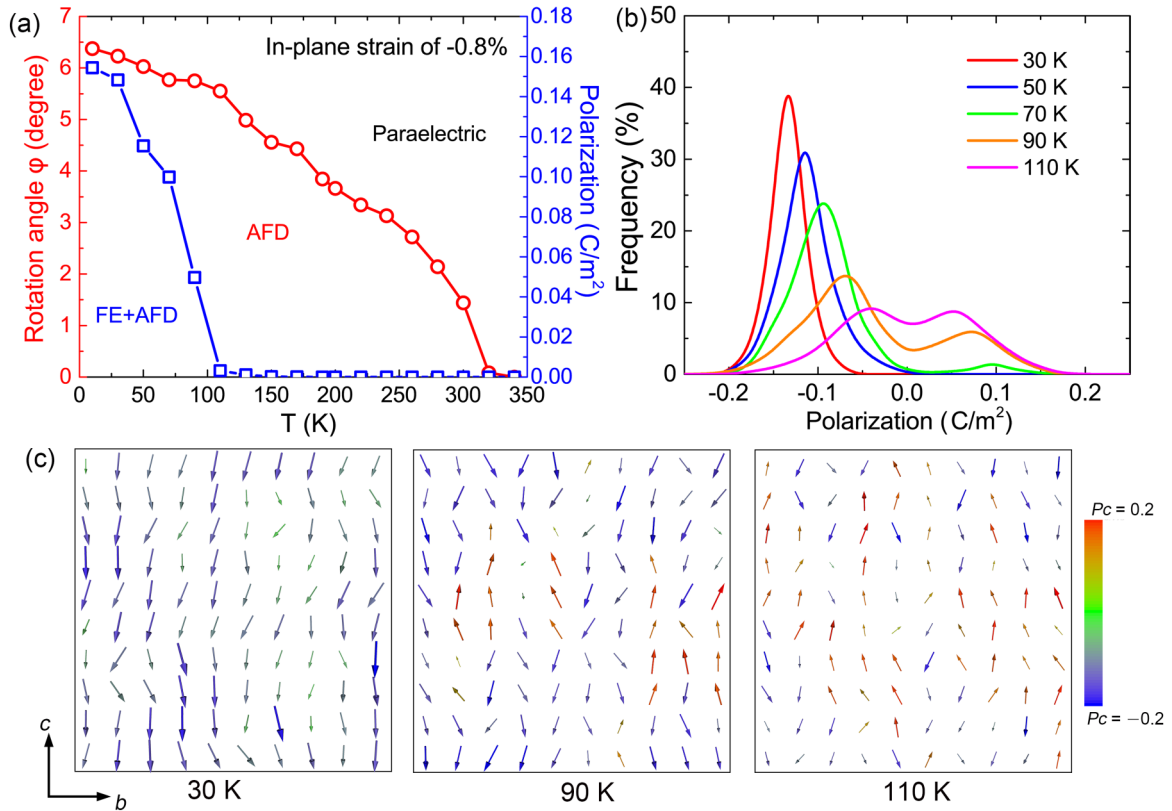
FIG. 8. Polarization (P) and rotation angle of the octahedra (φ) of 5000-atom supercell STO under -0.8% biaxial in-plane strain conditions. (a) P and φ as a function of temperature. (b) The probability distribution of the local P in unit cell along the [001] direction at different temperatures. (c) Typical snapshots of dipole configurations in the bc plane (out of plane) at different temperatures. Each arrow represents the local electric dipole vector along out-of-plane within a pseudocubic unit cell.

transition increases almost linearly with strain ($\varepsilon > 0.2\%$), which agrees well with the experimentally measured T_c under tensile strain [17]. Following the DP model-predicted trend, one can estimate that the temperature of the FE transition can be above room temperature with tensile strain of 1.4% and compressive strain of 2.3%. This result agrees with room-temperature ferroelectricity of STO observed in experiments [16,17,58]. DPMD simulations also clarify that the wide region of possible FE transition range in the temperature-strain phase diagram predicted by the LDG model is the AFD phase [11,13]. In addition, it is interesting to note that the previously reported pure FE phase ($P \neq 0$ and $\varphi = 0$) was not observed in our phase diagram [10,11].

We further investigate the nature of the temperature-driven FE phase transition in compressively strained STO (strain of -0.8%). We calculated the average φ and P as a function of temperature using DPMD simulations with results shown in Fig. 8(a). It clearly reveals that the polarization and AFD structure coexist in the STO <110 K, and the polarization is induced by the off-centered displacement of Ti atoms and oxygen octahedron. The details of such an atomic structure are shown in Fig. S4 in the Supplemental Material [48]. Also, the DPMD simulations indicate that the polarization magnitude decreases with temperature and becomes zero above a FE phase transition temperature of 110 K. Like the polarization case, the AFD structure (i.e., φ) also disappears >320 K. To get the atomistic detail characteristics of the temperature-driven FE phase transition, we calculate the distribution of

local polarization of the c-axis component in the STO supercell at different temperatures, and the results are shown in Fig. 8(b). At 30 K, the distribution of local polarization in FE phase exhibits a single peak is located near ~ -0.14 C/m^2. The corresponding snapshot of dipole configurations in the bc plane (out-of-plane) are shown in Fig. 8(c), indicating long-range polarization order along the c axis in the FE phase. As the temperature increases, the peak shifts to the lower value, suggesting a displacive FE phase transition. When the temperature further rises to 90 and 110 K, another peak emerged at the opposite position, indicating the reversal of the polarization vector [see dipole configurations of 90 and 110 K in Fig. 8(c)]. It demonstrates that the FE phase transition in STO under strain has both displacive and order-disorder characteristics. These results are in line with the theoretical and latest experiment studies that the FE phase transition in STO under strain has the mixture of displacive and order-disorder characteristics [17,59,60]. Similar characteristics of phase transition are also found in tensile strained STO (see Fig. S6 in the Supplemental Material [48]).

IV. CONCLUSIONS

In summary, we developed the DP model to describe dynamic and energetic properties of STO and its structural transition with the accuracy of DFT at the PBEsol level. After confirming the accuracy of the DP model by comparison of the lattice constant, free energy, and other properties with

DFT calculation results, we used the DP model to simulate temperature-driven tetragonal-to-cubic phase transition at the finite temperature. Then we predict the in-plane biaxial strain-temperature phase diagram of STO using the DP model and get the atomistic insights into the FE and AFD structural transitions. We clarify that the FE phase at low temperatures under strain is associated with AFD. With the temperature increasing, such an FE phase transforms into the AFD phase. Moreover, it is demonstrated that the FE phase transition in STO under strain has characteristics of both displacive and order-disorder phase transitions. These simulations provide insights into the behavior of the FE phase transition of STO. Ultimately, the machine learning method provides significant promise for the successful development of interatomic potentials for more complex perovskite materials.

[1] C. Zener, Phys. Rev. **82**, 403 (1951).

[2] G. Hodes, Science **342**, 317 (2013).

[3] D. D. Fong, G. B. Stephenson, S. K. Streiffer, J. A. Eastman, O. Auciello, P. H. Fuoss, and C. Thompson, Science **304**, 1650 (2004).

[4] A. Ohtomo and H. Hwang, Nature (London) **427**, 423 (2004).

[5] Z. S. Popović, S. Satpathy, and R. M. Martin, Phys. Rev. Lett. **101**, 256801 (2008).

[6] A. F. Santander-Syro, O. Copie, T. Kondo, F. Fortuna, S. Pailhès, R. Weht, X. G. Qiu, F. Bertran, A. Nicolaou, A. Taleb-Ibrahimi *et al.*, Nature (London) **469**, 189 (2011).

[7] A. D. Caviglia, M. Gabay, S. Gariglio, N. Reyren, C. Cancellieri, and J. M. Triscone, Phys. Rev. Lett. **104**, 126803 (2010).

[8] M. Ben Shalom, M. Sachs, D. Rakhmilevitch, A. Palevski, and Y. Dagan, Phys. Rev. Lett. **104**, 126802 (2010).

[9] Z. Zhong, A. Tóth, and K. Held, Phys. Rev. B **87**, 161102 (2013).

[10] Q.-Y. Wang, Z. Li, W.-H. Zhang, Z.-C. Zhang, J.-S. Zhang, W. Li, H. Ding, Y.-B. Ou, P. Deng, K. Chang *et al.*, Chin. Phys. Lett. **29**, 037402 (2012).

[11] J.-F. Ge, Z.-L. Liu, C. Liu, C.-L. Gao, D. Qian, Q.-K. Xue, Y. Liu, and J.-F. Jia, Nat. Mater. **14**, 285 (2015).

[12] W. Zhong and D. Vanderbilt, Phys. Rev. Lett. **74**, 2587 (1995).

[13] P. Fleury, J. Scott, and J. Worlock, Phys. Rev. Lett. **21**, 16 (1968).

[14] K. A. Müller and H. Burkard, Phys. Rev. B **19**, 3593 (1979).

[15] W. Zhong and D. Vanderbilt, Phys. Rev. B **53**, 5047 (1996).

[16] J. H. Haeni, P. Irvin, W. Chang, R. Uecker, P. Reiche, Y. L. Li, S. Choudhury, W. Tian, M. E. Hawley, B. Craigo *et al.*, Nature (London) **430**, 758 (2004).

[17] R. Xu, J. Huang, E. S. Barnard, S. S. Hong, P. Singh, E. K. Wong, T. Jansen, V. Harbola, J. Xiao, B. Y. Wang *et al.*, Nat. Commun. **11**, 3141 (2020).

[18] R. He, J. L. Lin, Q. Liu, Z. Liao, L. Shui, Z. J. Wang, Z. Zhong, and R.-W. Li, ACS Appl. Mater. Interfaces **12**, 45602 (2020).

[19] D. Lee, H. Lu, Y. Gu, S.-Y. Choi, S.-D. Li, S. Ryu, T. R. Paudel, K. Song, E. Mikheev, S. Lee *et al.*, Science **349**, 1314 (2015).

[20] T. Mitsui and W. B. Westphal, Phys. Rev. **124**, 1354 (1961).

[21] T. F. Nova, A. S. Disa, M. Fechner, and A. Cavalleri, Science **364**, 1075 (2019).

[22] X. Li, T. Qiu, J. Zhang, E. Baldini, J. Lu, A. M. Rappe, and K. A. Nelson, Science **364**, 1079 (2019).

[23] S. Hayward and E. Salje, Phase Transitions **68**, 501 (1999).

[24] N. Pertsev, A. Tagantsev, and N. Setter, Phys. Rev. B **61**, R825 (2000).

[25] Y. Li, S. Choudhury, J. Haeni, M. Biegalski, A. Vasudevarao, A. Sharan, H. Ma, J. Levy, V. Gopalan, and S. Trolier-McKinstry, Phys. Rev. B **73**, 184112 (2006).

[26] H. Uwe and T. Sakudo, Phys. Rev. B **13**, 271 (1976).

[27] R. Wahl, D. Vogtenhuber, and G. Kresse, Phys. Rev. B **78**, 104116 (2008).

[28] S. E. Reyes-Lillo, K. M. Rabe, and J. B. Neaton, Phys. Rev. Materials **3**, 030601 (2019).

[29] R. B. Wexler, Y. Qi, and A. M. Rappe, Phys. Rev. B **100**, 174109 (2019).

[30] S. Tinte, M. Stachiotti, S. Phillpot, M. Sepliarsky, D. Wolf, and R. Migoni, J. Phys.: Condens. Matter **16**, 3495 (2004).

[31] T. Katsumata, Y. Inaguma, M. Itoh, and K. Kawamura, Solid State Ionics **108**, 175 (1998).

[32] J. Behler and M. Parrinello, Phys. Rev. Lett. **98**, 146401 (2007).

[33] A. P. Bartók, M. C. Payne, R. Kondor, and G. Csányi, Phys. Rev. Lett. **104**, 136403 (2010).

[34] Y. Zhao, J. Fan, L. Su, T. Song, S. Wang, and C. Qiao, in *2020 IEEE 40th International Conference on Distributed Computing Systems (ICDCS)* (IEEE, Singapore, 2020), pp. 584–594.

[35] K. T. Schütt, H. E. Sauceda, P.-J. Kindermans, A. Tkatchenko, and K.-R. Müller, J. Chem. Phys. **148**, 241722 (2018).

[36] L. Zhang, J. Han, H. Wang, R. Car, and E. Weinan, Phys. Rev. Lett. **120**, 143001 (2018).

[37] L. Zhang, J. Han, H. Wang, W. A. Saidi, R. Car, and E. Weinan, End-to-end symmetry preserving inter-atomic potential energy model for finite and extended systems, in *Proceedings of the 32nd International Conference on Neural Information Processing Systems*, NIPS'18 (Curran Associates, Inc., Red Hook, NY, 2018), pp. 4441–4451.

[38] J. Wu, Y. Zhang, L. Zhang, and S. Liu, Phys. Rev. B **103**, 024108 (2021).

[39] Y. Zhang, H. Wang, W. Chen, J. Zeng, L. Zhang, H. Wang, and E. Weinan, Comput. Phys. Commun. **253**, 107206 (2020).

[40] J. Wu, L. Bai, J. Huang, L. Ma, J. Liu, and S. Liu, Phys. Rev. B **104**, 174107 (2021).

[41] J. Huang, L. Zhang, H. Wang, J. Zhao, J. Cheng, and E. Weinan, J. Chem. Phys. **154**, 094703 (2021).

[42] L. Zhang, D.-Y. Lin, H. Wang, R. Car, and E. Weinan, Phys. Rev. Materials **3**, 023804 (2019).

[43] N. Xu, Y. Shi, Y. He, and Q. Shao, J. Phys. Chem. C **124**, 16278 (2020).

[44] L. Zhang, H. Wang, R. Car, and E. Weinan, Phys. Rev. Lett. **126**, 236001 (2021).

[45] G. Kresse and J. Furthmüller, Comput. Mater. Sci. **6**, 15 (1996).

[46] G. Kresse and J. Furthmüller, Phys. Rev. B **54**, 11169 (1996).

[47] J. P. Perdew, K. Burke, and M. Ernzerhof, Phys. Rev. Lett. **78**, 1396 (1997).

[48] See Supplemental Material at http://link.aps.org/supplemental/10.1103/PhysRevB.105.064104 for Table S1 and Figs. S1–S6.

[49] S. Plimpton, J. Comput. Phys. **117**, 1 (1995).

[50] M. Parrinello and A. Rahman, J. Appl. Phys. **52**, 7182 (1981).

[51] S. Nosé, J. Chem. Phys. **81**, 511 (1984).

[52] T. Riste, E. J. Samuelsen, K. Otnes, and J. Feder, Solid State Commun. **9**, 1455 (1971).

[53] A. Okazaki and M. Kawaminami, Mater. Res. Bull. **8**, 545 (1973).

[54] H. Dammak, Y. Chalopin, M. Laroche, M. Hayoun, and J.-J. Greffet, Phys. Rev. Lett. **103**, 190601 (2009).

[55] H. Dammak, M. Hayoun, F. Brieuc, and G. Geneste, J. Phys. Conf. Ser. **1136**, 012014 (2018).

[56] J.-L. Barrat and D. Rodney, J. Stat. Phys. **144**, 679 (2011).

[57] H. Vogt, Phys. Rev. B **51**, 8046 (1995).

[58] T. Li, S. Deng, H. Liu, S. Sun, H. Li, S. Hu, S. Liu, X. Xing, and J. Chen, Adv. Mater. **33**, 2008316 (2021).

[59] A. Bussmann-Holder, H. Beige, and G. Völkel, Phys. Rev. B **79**, 184111 (2009).

[60] S. Salmani-Rezaie, K. Ahadi, W. M. Strickland, and S. Stemmer, Phys. Rev. Lett. **125**, 087601 (2020).